remote sensing

MDPI

Article

Multiple-Input Multiple-Output Synthetic Aperture Radar Waveform and Filter Design in the Presence of Uncertain Interference Environment

Ke Xu [1], Guohao Sun [1,2,*], Yuandong Ji [1], Zhiquan Ding [3,4] and Wenhao Chen [3]

[1] School of Aeronautics and Astronautics, Sichuan University, Chengdu 610065, China; lvwenjie@stu.scu.edu.cn (K.X.); jyd1127@scu.edu.cn (Y.J.)
[2] Robotic Satellite Laboratory, Chengdu 610065, China
[3] Sichuan Institute of Aerospace Electronic Equipment, Chengdu 610199, China; dingzhiquan@7105.scaic.casc (Z.D.); chenwenhao@7105.scaic.casc (W.C.)
[4] Multi-Source Information Intelligent Fusion Key Laboratory of Sichuan Province, Chengdu 610016, China
* Correspondence: sgh2019@scu.edu.cn

Abstract: Multiple-input multiple-output synthetic aperture radar (MIMO-SAR) anti-jamming waveform design relies on accurate prior information about the interference. However, it is difficult to obtain accurate prior knowledge about uncertain intermittent sampling repeater jamming (ISRJ), leading to a severe decline in the detection performance of MIMO-SAR systems. Therefore, this article studies the robust joint design problem of MIMO radar transmit waveform and filter against uncertain ISRJ. We characterize two categories of uncertain interference, including sample length uncertainty and sample-time uncertainty, modeled as Gaussian distribution in different range bins. Based on the uncertain interference model, we formulate the maximizing SINR as a figure of merit, which is a non-convex quadratic optimization problem under specific waveform constraints. Based on the alternating direction method of multipliers (ADMM) framework, a novel joint design algorithm of waveform and filter is proposed. In order to improve the convergence performance of ADMM, the difference in convex functions (DC) programming is applied to the ADMM iterations framework to solve the problem of waveform energy inequality constraint. Finally, numerical results demonstrate the effectiveness and robustness of the proposed method, compared to the existing methods that utilize deterministic interference models in the uncertain ISRJ environment. Moreover, the spaceborne SAR real scene imaging simulations are conducted to evaluate the anti-ISRJ performance.

Keywords: MIMO-SAR; uncertain ISRJ; waveform design; filter design; ADMM algorithm

check for updates

Citation: Xu, K.; Sun, G.; Ji, Y.; Ding, Z.; Chen, W. Multiple-Input Multiple-Output Synthetic Aperture Radar Waveform and Filter Design in the Presence of Uncertain Interference Environment. *Remote Sens.* **2024**, *16*, 4413. https://doi.org/10.3390/rs16234413

Academic Editors: Mengdao Xing, Jianlai Chen, Yu Li and Yongkang Li

Received: 8 October 2024
Revised: 19 November 2024
Accepted: 20 November 2024
Published: 25 November 2024

Copyright: © 2024 by the authors. Licensee MDPI, Basel, Switzerland. This article is an open access article distributed under the terms and conditions of the Creative Commons Attribution (CC BY) license (https://creativecommons.org/licenses/by/4.0/).

1. Introduction

Multiple-input multiple-output synthetic aperture radar (MIMO-SAR) systems have a higher degree of freedom compared to traditional spaceborne SAR through the transmitting and receiving of multiple antennas. It has great advantages in wide mapping band high-resolution imaging, 3D imaging, multi-baseline interference, and clutter suppression [1–4]. Moreover, without increasing the pulse repetition frequency (PRF), MIMO-SAR radar can be applied in high-resolution imaging, the detection of slow-moving targets, and weak targets. In addition, the radar waveform design of MIMO-SAR can thereby effectively enhance the operational capabilities of the radar system (such as target detection, imaging, tracking, and anti-jamming) by continuously adjusting the transmit waveform [5,6]. Array synthetic aperture radar (SAR) 3D imaging can obtain 3D information of the target region, which is widely used in environmental monitoring and scattering information measurement [7,8]. Furthermore, novel 3D sparse reconstruction algorithms are proposed in [9].

Interference causes a significant threat to the performance of MIMO-SAR, especially intermittent sampling repeater jamming (ISRJ). It samples and forwards a small segment

of the radar pulse signal, rapidly alternating between short-time sampling and short-time forwarding until the entire radar pulse signal is completed [10,11]. ISRJ produced by the digital radio frequency memory (DRFM) technology makes the synthetic aperture radar (SAR) imagery confusing [12–14]. In the meanwhile, ISRJ resolves the issue of antenna isolation in engineering applications through time-division transmitting and receiving, while also enhancing interference response speed and enabling the formation of pre-guidance false targets. MIMO-SAR is significantly affected by ISRJ, as it intercepts radar signals through jamming devices, simulating similar echoes and generating false point targets in SAR images [15,16]. The radar system may treat false targets as real targets influenced by ISRJ, which causes parameter estimation and tracking performance deteriorate [17,18].

For deterministic interference, MIMO radar waveform design for multiple targets has been widely studied. The joint optimal design of the transmit waveform and filter is based on complete prior knowledge, especially for maximizing the signal-to-interference-plus-noise ratio (SINR) by deriving the expression. In [19], based on maximizing the SINR criterion, this article solves a non-convex optimization problem in the joint design of MIMO radar waveform and filter under three scenarios with different constraints. For the waveform energy constraint, the authors utilize an iterative algorithm to iteratively optimize the transmit waveform and filter until SINR converges. For constant mode constraint and similarity constraint, they transform the non-convex problem into a semi-definite programming (SDP) problem and a fractional problem and then solve them, respectively. In [20], the author adapts prior knowledge of the target and interference to construct a model of the maximization SINR problem. Compared to traditional iterative optimization algorithms, the authors combine the transmit waveform and the filter vector into a single variable, avoiding the computational complexity problem associated with quadratic optimization and initialization. An adaptive waveform design algorithm based on information theory is proposed to improve the efficiency of the multi-hypothesis testing in [21]. The authors adopt a semi-definite relaxation technique and semi-definite programming to tackle the non-convex design problem based on relative entropy. Waveform optimization algorithm with similarity, energy, and CRB constraints is proposed in [22], which improves target detection performance with certain Doppler estimation accuracy. The aforementioned waveform design methods require precise prior knowledge to improve the performance of radar.

Existing methods are mainly aimed at the anti-interference waveform design of deterministic interference. For example, in [23], a non-convex joint design problem for transmit waveform and receive filter is studied with ISRJ, which is solved based on the ADPM framework. In [24], the joint design problem under multiple constraints is formulated with the optimization criterion of minimizing the integrated sidelobe levels (ISLs) of waveform mismatch filter output and integrated levels (ILs) of ISRJ signal mismatch filter output. In [25], the authors deal with the joint design problem for pulse initial phase optimization, which suppresses velocity deception interference by controlling the false target echo spectrum to form a zero-trapping within a certain range. In [26], orthogonal block-coded signals are designed to realize interference suppression. In [27], a variety of examples related to waveform design, considering both signal-independent and signal-dependent interferences, have been compiled, including scenarios such as multipath interference, clutter, and internal thermal noise. To realize the suppression of velocity deception interference under single/multiple target detection, a waveform design method used multi-channel processing with different integer multiple pulse repetition intervals (PRI) with adaptive initial phase proposed in [28]. The above waveform design algorithms perform against specific interference instead of uncertain ISRJ.

The uncertain ISRJ refers to the jamming signal obtained after intermittently and non-uniformly sampling the radar transmit signal. The randomness of uncertain ISRJ is reflected in two aspects. The sample length uncertainty and sample-time uncertainty of the interference affect the magnitude size and spatial distribution of the false targets [29].

Sample-time uncertainty affects false target locations, intervals, and numbers. The smaller the intermittent sampling period and the larger the false target interval, the fewer the number of false targets in a finite field of view [30,31]. Furthermore, the sample length uncertainty changes the duty cycle of the interference, while the duty cycle affects the false target amplitude. The false target amplitude changes with the duty cycle. Concurrently, the magnitude of each false target within sub-false target groups diminishes at a more rapid rate, resulting in the formation of clusters of false targets with considerable discrepancies in magnitude [32]. Furthermore, the uncertain ISRJ process alters the uniform characteristics of the false target groups, thereby increasing the difficulty of radar detection of false targets. An intermittent non-uniform interval sampling forwarding interference method based on the taboo search algorithm is proposed in [33]. The method generates multiple false targets, creating a suppression-like interference effect through non-uniform interval sampling in the time domain and an indefinite number of repetitions. In [34], the author generates non-uniformly sampled pulses by using pseudo-random sequences. It obtains the interference by repeatedly transmitting the sampling signal. With prior knowledge of target statistics and clutter statistics, by modeling clutter with respect to its Gaussian distribution characteristics, studying the MIMO space-time adaptive processing (MIMO-STAP) radar for robust detection of ground-moving targets under target and clutter uncertainty, the joint design problem of transmit waveform and receive filter is proposed in [35]. The difficulties of waveform design in uncertain interference environments are mainly reflected in many aspects. The parameters of uncertain ISRJ are variable, which creates difficulty in acquiring prior knowledge. In order to design an appropriate waveform for uncertain interference and to improve the robustness of waveform in an uncertain interference environment, we need to accurately characterize a class of uncertain interferences with partial prior knowledge. Moreover, the constraints in the waveform design problem lead to the joint optimization problem model being a non-convex problem.

In this article, we study the uncertain ISRJ in the complex interference environment [36] and improve the robustness of the waveform by iteratively co-designing the transmit waveform and receive filter. To address the above difficulties, the main contributions of this article are summarized as follows:

1. An uncertain ISRJ model is established, describing two typical Gaussian uncertain interference. Uncertain interference's Gaussian distribution characteristics of the sample-length and sample-time uncertainty are modeled as a random distribution. Specifically, based on partially prior knowledge about interference parameters, the uncertain ISRJ model is established for the two main features of slice width and sampling period, and its model is adapted to solve the optimal transmit waveform.
2. The problem of robust joint design of transmit waveform and receive filter for MIMO radar in uncertain interference environment is solved based on ADMM. Especially for the non-convexity of the constant waveform energy constraints, the DC algorithm enhances the convergence of ADMM. Meanwhile, for the non-constant waveform energy constraints, the DC-based algorithm is designed.

2. Models of Randomized Store-and-Forward Interference and Waveform Design

In this section, we develop the waveform and filter model that describes two types of different uncertain interference, and propose a model for the waveform robust design optimization problem under an uncertain ISRJ environment.

2.1. Signal Model

Consider a MIMO-SAR system with N_T transmit antennas and N_R receive antennas. Assume that the radar system transmits a burst of pulses in a coherent processing interval (CPI) with a constant pulse repetition. $\mathbf{S} = [\mathbf{s}(1), \mathbf{s}(2), \cdots, \mathbf{s}(L)] \in \mathbb{C}^{N_T \times L}$ represents the

radar transmit waveform with the code length L. Then the target signal echo of the Mth pulse can be expressed as

$$\mathbf{Y}_{tar,m} = \alpha_t e^{j2\pi(m-1)f_d}\mathbf{a}_r(\theta_t)\mathbf{a}_t^T(\theta_t)\mathbf{S} \tag{1}$$

where $m = 1, 2, \ldots, M$, α_t is the amplitude, $f_d = 2v_d T_r/\lambda$ is the normalized target Doppler frequency, and $T_r = 1/f_r$ represents the pulse repetition period. Meanwhile, λ is the carrier wavelength, and $\mathbf{a}_r(\theta_t)$, $\mathbf{a}_t(\theta_t)$ are the transmit steering and receive steering vectors, respectively.

For convenience, stacking all the columns of target echo $\mathbf{Y}_{tar,m}$ into a vector, we have

$$\begin{aligned}\mathbf{y}_{tar} &= \left[\mathrm{vec}^T\left(\mathbf{Y}_{t,1}^T\right), \mathrm{vec}^T\left(\mathbf{Y}_{t,2}^T\right), \cdots, \mathrm{vec}^T\left(\mathbf{Y}_{t,M}^T\right)\right]^T \\ &= \alpha_t\left(\mathbf{I}_M \otimes \mathbf{I}_{N_R} \otimes \mathbf{S}^T\right)\mathbf{v}_t\end{aligned} \tag{2}$$

where $\mathbf{v}_t = \mathbf{u}(f_d) \otimes \mathbf{a}_r(\theta_t) \otimes \mathbf{a}_t(\theta_t)$.

$\mathbf{u}(f_d) = \left[1, e^{j2\pi f_d}, \cdots, e^{j2\pi(M-1)f_d}\right]^T \in \mathbb{C}^{M\times 1}$ is the temporal steering vector. Then, consider the filter $\mathbf{W} = [\mathbf{w}_1, \mathbf{w}_2, \cdots, \mathbf{w}_L]^T \in \mathbb{C}^{L\times MN_R}$, and its vectorization is $\mathbf{w} = \mathrm{vec}(\mathbf{W}) \in \mathbb{C}^{LMN_R\times 1}$.

2.2. Model of ISRJ with Uncertain Sample Length

The following jamming signal model is

$$\mathbf{S}_J = \mathbf{J}_e\mathbf{S} \tag{3}$$

where $\mathbf{J}_e = \mathrm{diag}(\mathbf{j}) \in \mathbb{R}^{L\times L}$ is the store-and-forward matrix, and $\mathbf{j}$ is a vector satisfying a 0/1 random distribution, which determines the characteristics of the interference sampling signal.

Considering the store-and-forward mechanism of complex uncertain interference with uncertain sample length, the store-and-forward matrix of interference can be represented by the following formula [23,37]:

$$\mathbf{J}_e = \begin{bmatrix} \mathbf{A}_{t_1} & \mathbf{0} & \cdots & \mathbf{0} \\ \mathbf{0} & \mathbf{A}_{t_2} & & \vdots \\ \vdots & & \ddots & \mathbf{0} \\ \mathbf{0} & \cdots & \mathbf{0} & \mathbf{A}_{t_m} \end{bmatrix}_{L\times L} \tag{4}$$

where $m = 1, 2, \ldots, M$. $M = \lfloor T_p/t_s \rfloor$ represents the number of pulses, where T_p and t_s are the pulse width of radar transmit signal and the sample interval of jammer. Each dimension of $\mathbf{A}_t$ is the same because they have a common sampling period. The uncertainty of sample length is mainly reflected in the difference in elements in $\mathbf{A}_t$, which is specifically defined as follows:

$$\mathbf{A}_{t_m} = \begin{bmatrix} \mathbf{I}_{b_m} & 0 \\ 0 & 0 \end{bmatrix}_{N_s\times N_s} \tag{5}$$

where $N_s = \lfloor T_s/t_s \rfloor$. The dimension of the unit matrix $\mathbf{I}_b$ in $\mathbf{A}_t$ is randomized, which is determined by $b = \lfloor (T_s \pm \varepsilon)/t_s \rfloor$. ε follows a Gaussian distribution with mean μ and variance σ^2 [29], which is denoted by $\varepsilon \sim N(\mu, \sigma^2)$. It also constitutes a randomization of the sample length in the presence of complex interference.

The radar interferer samples the received transmit signal randomly and continuously. Each sample intercepts an indeterminate number of sub-segments, i.e., the dimension of the unit array $\mathbf{I}_t$ in the $\mathbf{J}_e$ matrix is indeterminate. It corresponds to the different widths T_L of neighboring sampled segments in Figure 1a. The red and orange background colors emphasise the variability of the parameters. Sample-time uncertainty is the randomness of

the time interval between two adjacent sampling starting points, which means that $\mathbf{I}_t$ occurs on the diagonal in an indeterminate position. It corresponds to different T_s in Figure 1b. Considering the uncertainties of the two sampling methods together, as shown in Figure 1c, uncertain sample length and sample time constitute a non-regular characteristic of the store-and-forward method. Random interference produces a false target within a small area of the interference slice sample, causing the real target to be submerged and creating serious disturbance to target identification of the radar system. It is difficult for radar systems to categorize the interference and develop appropriate anti-interference strategies. Therefore, random interference is threatening to modern radar systems.

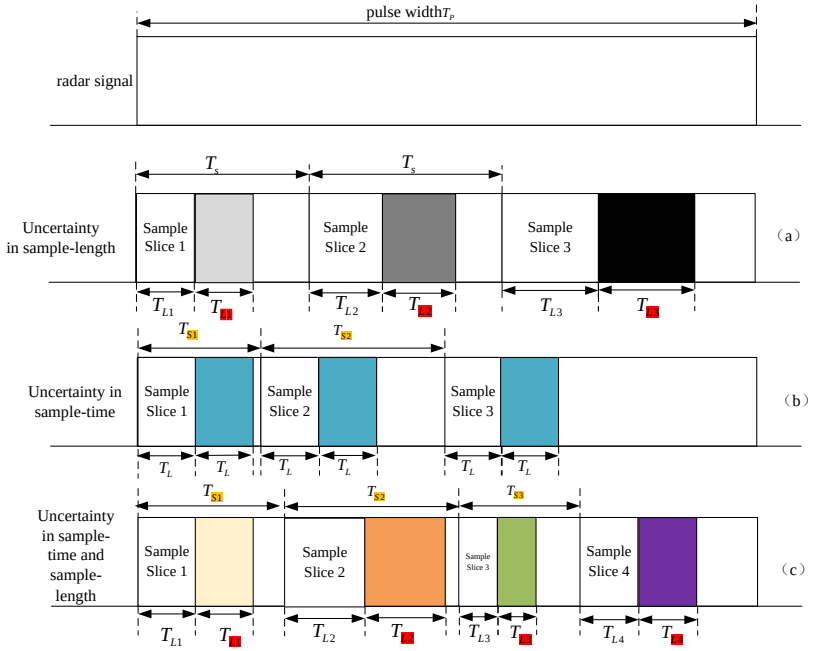


Figure 1. Uncertain store-and-forward schematic. (**a**) sample-length; (**b**) sample-time; (**c**) sample-length and sample-time.

2.3. Model of ISRJ with Uncertain Sample Time

Consider the randomness of the sample time in Figure 1, The definition of $\mathbf{J}_e$ is the same as the sample-length uncertainty model; $\mathbf{A}_t$ is defined as follows:

$$\mathbf{A}_t = \begin{bmatrix} \mathbf{I}_c & 0 \\ 0 & 0 \end{bmatrix}_{N_R \times N_R} \tag{6}$$

where the size of N_R is determined by the interval $T_{s_1}, T_{s_2}, \ldots$ between adjacent samples. $\mathbf{I}_c$ is a unit matrix with defined dimensions. Specifically, its dimension is determined by sample duration T_L and sub-pulse width of code t_s.

$\mathbf{J}_t$ is the shift matrix, which represents the offset of the interference signal compared to the target position range ring. If the target is located at the r-th range bin, then

$$\mathbf{J}_t(i,j) = \begin{cases} 1, \text{if} & i-j+l=0 \\ 0, \text{if} & i-j+l \neq 0 \end{cases} \quad (i,j) \in \{1,2,\ldots,L\}^2 \tag{7}$$

When the source of interference is in the same range bin as the target, the interference signal is not shifted compared to the target signal, i.e., $\mathbf{J}_t = \mathbf{I}$. The remaining cases are the corresponding sub-diagonal matrices.

The reasons for the uncertainty in the sample time include the fact that the location of the interference source is not estimated correctly. Without loss of generality, the estimated position error follows a Gaussian distribution. The location distribution of the interference in the vicinity of the target range bin satisfies the discrete Gaussian distribution, as shown

in Figure 2. Considering a total of $2P+1$ range bins in the vicinity of the target [19], the estimated position of the target in Figure 2 obeys a Gaussian distribution around the true position [38]. The deviation of the position of the true value from the estimated value can be described in terms of the range bins associated with the shift matrix. The probability p is used to estimate the likelihood of the interference appearing in the corresponding range bin, respectively. In summary, the interference signal echo of the g-th interference, m-th pulse is defined as $\mathbf{Y}_{j,g,m} = \alpha_g e^{j2\pi(m-1)f_g}\mathbf{a}_r(\theta_g)\mathbf{a}_t{}^T(\theta_g)\mathbf{S}\mathbf{J}_g$. α_g, f_g, and θ_g denote the complex amplitude, normalized Doppler frequency, and direction of arrival of the g-th interference, respectively. $\mathbf{J}_g$ is the product of the shift matrix and the store-and-forward matrix, where $\mathbf{J}_g = \mathbf{J}_t\mathbf{J}_e \in \mathbf{R}^{L\times L}$. The store-and-forward mechanism of jammer dictates $\mathbf{J}_e$. In the meanwhile, $\mathbf{J}_t$ expresses the uncertainty in the spatial distribution of the interference signal.

The random probability matrix is defined as

$$\mathbf{P} = \mathrm{E}[\mathrm{vec}(\mathbf{J}_e\mathbf{J}_t)\mathrm{vec}^{\mathrm{H}}(\mathbf{J}_e\mathbf{J}_t)] \tag{8}$$

where $\mathbf{P}$ represents the statistical matrix of the probability distribution of random interference [39]. Briefly, we construct $\mathbf{P}$ that can be used to describe various types of store-and-forward mechanisms.

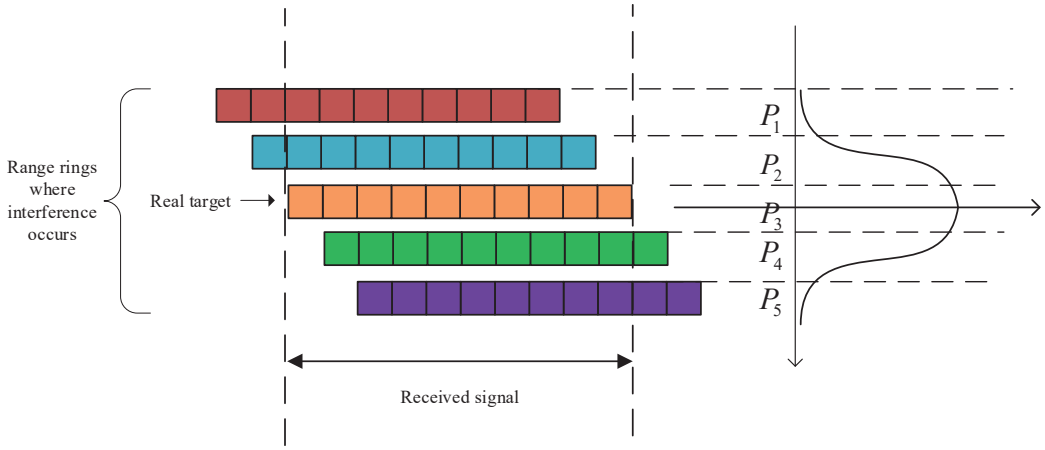


Figure 2. Schematic representation of the uncertainty in the location of the source of interference.

The store-and-forward matrix is coupled to the shift matrix associated with the range bin, and we can't consider their respective expectations. So, using $\mathrm{vec}(\mathbf{AB}) = (\mathbf{I}\otimes\mathbf{A})\mathrm{vec}(\mathbf{B})$, we have

$$\begin{aligned}&\mathrm{E}\left[\mathrm{vec}(\mathbf{J}_e\mathbf{J}_t)\mathrm{vec}^{\mathrm{H}}(\mathbf{J}_e\mathbf{J}_t)\right]\\&= (\mathbf{I}\otimes\mathrm{E}[\mathbf{J}_e])\left(\mathrm{vec}(\mathrm{E}[\mathbf{J}_t])\mathrm{vec}^{H}(\mathrm{E}[\mathbf{J}_t])\right)\left(\mathbf{I}\otimes\mathrm{E}\left[\mathbf{J}_e{}^{H}\right]\right)\end{aligned} \tag{9}$$

then, the received interfering vector $\mathbf{y}_j$ can be expressed as the superposition of the returns from interference sources, i.e.,

$$\mathbf{y}_j = \sum_{g=1}^{G}\alpha_g(\mathbf{I}_M\otimes\mathbf{I}_{N_R}\otimes(\mathbf{S}\mathbf{J}_g)^{\mathrm{T}})\mathbf{v}_g \tag{10}$$

where $\mathbf{v}_g = \mathbf{u}(f_g)\otimes\mathbf{a}_r(\theta_g)\otimes\mathbf{a}_t(\theta_g)$. f_g denotes the Doppler frequency of the interference signal.

The total received signal vector in a CPI can be modeled as

$$\mathbf{y} = \mathbf{y}_{tar} + \mathbf{y}_j + \mathbf{n} \tag{11}$$

where $\mathbf{n} \sim N(0, \sigma^2\mathbf{I}_{LMN_R})$ is the signal-independent noise vector.

2.4. Model of Joint Waveform and Filter Design Problem

This part presents the problem of robust joint design of transmit waveform and receive filter for the interference environment of MIMO radar systems, so as to maximize the output SINR under specific constraints.

Let $\mathbf{W} = [\mathbf{w}_1, \mathbf{w}_2, \ldots, \mathbf{w}_L]^T \in \mathbb{C}^{L \times MN_R}$; $\mathbf{w} = \mathrm{vec}(\mathbf{W}) \in \mathbb{C}^{LMN_R \times 1}$ denotes the filter after vectorization. Then, the output SINR of the objective optimization function can be given by

$$\mathrm{SINR} = \frac{\left|\mathbf{w}^H \mathbf{y}_t\right|^2}{\mathbf{w}^H \mathrm{E}(\mathbf{y}_j \mathbf{y}_j{}^H + \mathbf{n}\mathbf{n}^H)\mathbf{w}} \tag{12}$$

The numerator of (12) represents the useful energy at the output of the receive filter, while the denominator represents the interference energy and noise energy. Using $\mathbf{w}^H E\left(\mathbf{y}_j \mathbf{y}_j^H\right)\mathbf{w} = E\left(\left|\mathbf{y}_j^H \mathbf{w}\right|^2\right)$ and $\mathbf{w}^H E\left(\mathbf{n}\mathbf{n}^H\right)\mathbf{w} = \sigma^2 \mathbf{w}^H \mathbf{w}$, we have

$$\begin{aligned} \mathrm{SINR} &= \frac{\left|\mathbf{w}^H \mathbf{y}_t\right|^2}{\mathbf{w}^H \mathrm{E}(\mathbf{y}_j \mathbf{y}_j^H + \mathbf{n}\mathbf{n}^H)\mathbf{w}} \\ &= \frac{\alpha_t^2 \mathbf{w}^H (\mathbf{I}_{MN_R} \otimes \mathbf{S}^T)\mathbf{v}_t \mathbf{v}_t^H (\mathbf{I}_{MN_R} \otimes \mathbf{S}^*)\mathbf{w}}{\mathbf{w}^H [\sum_{g=1}^{G} [(\alpha_g \mathbf{V}_g^T \mathbf{S} \otimes \mathbf{I})\mathbf{P}(\alpha_g \mathbf{S}^H \mathbf{V}_g^* \otimes \mathbf{I})] + \sigma^2 \mathbf{I}]\mathbf{w}} \end{aligned} \tag{13}$$

after that, we deform the interference term and have

$$\begin{aligned} &\mathbf{w}^H \mathrm{E}[\mathbf{y}_j \mathbf{y}_j{}^H]\mathbf{w} \\ &= \sum_{g=1}^{G} \alpha_g^2 \mathrm{E}[\mathbf{w}^H \mathbf{\Sigma} \mathbf{\Lambda} \mathbf{\Sigma}^H \mathbf{w}] \end{aligned} \tag{14}$$

where $\mathbf{\Sigma} = \mathbf{I}_{MN_R} \otimes \mathbf{J}_g \mathbf{S}^T$, $\mathbf{\Lambda} = \mathbf{v}_g \mathbf{v}_g^H$. Deforming $\mathbf{\Sigma}^H \mathbf{w}$, we obtain

$$\begin{aligned} \mathbf{\Sigma}^{\mathrm{H}} \mathbf{w} &= (\mathbf{I} \otimes \mathbf{S}^* \mathbf{J}_g)\mathbf{w} = (\mathbf{W}_{MN_R \times L} \mathbf{J}_g \otimes \mathbf{I})\mathbf{s}^* \\ \mathbf{w}^{\mathrm{H}} \mathbf{\Sigma} &= \mathbf{s}^{\mathrm{H}} (\mathbf{J}_g{}^{\mathrm{H}} \mathbf{W}^{\mathrm{H}}{}_{MN_R \times L} \otimes \mathbf{I}) \end{aligned} \tag{15}$$

Substitute $\mathbf{w}^{\mathrm{H}} \mathbf{\Sigma}$ and $\mathbf{\Sigma}^{\mathrm{H}} \mathbf{w}$ into the SINR, which changes to

$$\begin{aligned} \mathrm{SINR} &= \frac{\left|\mathbf{w}^H \alpha_t (\mathbf{I}_M \otimes \mathbf{I}_{N_R} \otimes \mathbf{S}^T)\mathbf{v}_t\right|^2}{\mathbf{w}^H \mathrm{E}(\mathbf{y}_j \mathbf{y}_j^H + \mathbf{n}\mathbf{n}^H)\mathbf{w}} \\ &= \frac{\alpha_t^2 \mathbf{s}^{\mathrm{T}} (\mathbf{W}^* \otimes \mathbf{I})\mathbf{v}_t \mathbf{v}_t^H (\mathbf{W}^T \otimes \mathbf{I})\mathbf{s}^*}{\mathbf{s}^{\mathrm{T}} [\sum_{g=1}^{G} [(\mathbf{I} \otimes \alpha_g \mathbf{V}_g \mathbf{W}^H)\mathbf{P}(\mathbf{I} \otimes \alpha_g \mathbf{W} \mathbf{V}_g^H)] + \frac{\sigma^2}{\sigma_s^2} \mathbf{I}_{LMN_R}]\mathbf{s}^*} \end{aligned} \tag{16}$$

where $\mathbf{P} = \mathrm{E}[\mathrm{vec}(\mathbf{J}_g)\mathrm{vec}^{\mathrm{T}}(\mathbf{J}_g)]$ denotes the random probability matrix, σ and σ_s denote the noise variance and the mode of the waveform, respectively. The optimization problem for designing radar anti-interference transmit waveform using SINR maximization criterion can be given by

$$\begin{aligned} \max_{\mathbf{s}} \quad & \mathrm{SINR}(\mathbf{w}, \mathbf{s}) \\ \text{s.t.} \quad & \mathbf{s}^H \mathbf{s} \le 1 \\ & \|\mathbf{s} - \mathbf{s}_0\| \le \varepsilon \end{aligned} \tag{17}$$

where we consider low-energy constraint because of the demands of RF stealth. And we use similarity constraint to place limits on the waveform energy.

3. Robust Joint Design of MIMO Radar Waveform and Filter

3.1. Optimization of Transmit Waveform and Receive Filter Based on ADMM

The maximization of the output SINR with respect to $\mathbf{w}$ for a given $\mathbf{s}$ can be expressed as the following optimization problem:

$$\max_{\mathbf{w}} \frac{\mathbf{w}^H \mathbf{\Phi}(\mathbf{s}) \mathbf{w}}{\mathbf{w}^H \mathbf{\Phi}_{cn}(\mathbf{s}) \mathbf{w}} \tag{18}$$

Problem (18) is an unconstrained maximization problem, whose optimal solution can be obtained from the maximum generalized eigenvector of the matrices $\mathbf{\Phi}(\mathbf{s})$ and $\mathbf{\Phi}_{cn}(\mathbf{s})$; the optimal solution is [35]

$$\mathbf{w}_{opt} = \hbar((\mathbf{\Phi}_{cn}(\mathbf{s}))^{-1} \mathbf{\Phi}(\mathbf{s})) \tag{19}$$

where $\hbar(\cdot)$ denotes the generalized eigenvector with the largest generalized eigenvalue for the matrix. Then, by using the obtained optimal $\mathbf{w}_{opt}$, the transmit waveform with inequality and similarity constraints is optimized for maximizing the SINR.

Consider the following SINR objective function about waveform $\mathbf{s}$

$$\mathrm{SINR}(\mathbf{s}, \mathbf{w}) = \frac{\mathbf{s}^{\mathrm{H}} \mathbf{\Theta}(\mathbf{w}) \mathbf{s}}{\mathbf{s}^{\mathrm{H}} \mathbf{\Theta}_{\mathrm{cn}}(\mathbf{w}) \mathbf{s}} \tag{20}$$

Based on the principle of Dinkelbach's algorithm, the quadratic fractional form of the original objective function is transformed into a reduced form

$$f(\mathbf{s}, \mu) = \mathbf{s}^H (\mathbf{\Theta}(\mathbf{w}) - \mu \mathbf{\Theta}_{cn}(\mathbf{w})) \mathbf{s} \tag{21}$$

Summing up leads to the optimization problem

$$\begin{aligned} \min_{\mathbf{s}} \quad & \mathbf{s}^H (\mu \mathbf{\Theta}_{cn}(\mathbf{w}) - \mathbf{\Theta}(\mathbf{w})) \mathbf{s} \\ \text{s.t.} \quad & \mathbf{s}^H \mathbf{s} \leq 1 \\ & \|\mathbf{s} - \mathbf{s}_0\| \leq \varepsilon \end{aligned} \tag{22}$$

Problem (22) contains an energy constraint and a similarity constraint. Under the constrains, one cannot use the diagonal loading algorithm to transform the original non-convex problem into a convex one.Therefore, we consider a joint solution utilizing the DC-Programming algorithm with ADMM.

ADMM updates the dyadic variables alternately using a fixed penalty factor, which can be employed to decompose the objective function of the original problem into several of solvable subproblems. Then, it solves each subproblem in parallel and finally obtain the optimal solution of the original problem. Based on this framework, we introduce auxiliary variables $\mathbf{y}$, $\mathbf{z}$. Problem (22) equals

$$\begin{aligned} \min_{\mathbf{s},\mathbf{y},\mathbf{z}} \quad & \mathbf{s}^H (\mu \mathbf{\Theta}_{cn}(\mathbf{w}) - \mathbf{\Theta}(\mathbf{w})) \mathbf{s} \\ \text{s.t.} \quad & \mathbf{y}^H \mathbf{y} \leq 1 \\ & \mathbf{s} = \mathbf{y} \\ & \|\mathbf{z} - \mathbf{s}_0\| \leq \varepsilon \\ & \mathbf{s} = \mathbf{z} \end{aligned} \tag{23}$$

In the framework of ADMM, constraints can be combined into the augmented Lagrangian function; that is

$$\begin{aligned} L(\mathbf{s}, \mathbf{y}, \mathbf{z}, \boldsymbol{\lambda}, \boldsymbol{\gamma}) = & \mathbf{s}^H (\mu \mathbf{\Theta}_{cn}(\mathbf{w}) - \mathbf{\Theta}(\mathbf{w})) \mathbf{s} \\ & + \tfrac{\rho}{2} (\|\mathbf{s} - \mathbf{z} + \boldsymbol{\lambda}\|^2 - \|\boldsymbol{\lambda}\|^2) \\ & + \tfrac{\rho}{2} (\|\mathbf{s} - \mathbf{y} + \boldsymbol{\gamma}\|^2 - \|\boldsymbol{\gamma}\|^2) \end{aligned} \tag{24}$$

where ρ is the penalty parameter, and $\mathbf{y}$, $\mathbf{z}$ are auxiliary variables.

The waveform optimization design problem based on the ADMM algorithm can be described by the following iteration

$$\begin{cases} \text{step 1:} & \mathbf{s}^{t+1} = \arg\min_{\mathbf{s}} L(\mathbf{s}, \mathbf{y}^t, \mathbf{z}^t, \boldsymbol{\lambda}^t, \boldsymbol{\gamma}^t) \\ \text{step 2:} & \mathbf{y}^{t+1} = \arg\min_{\mathbf{y}} \left\| \mathbf{s}^{t+1} - \mathbf{y} + \boldsymbol{\gamma}^t \right\|^2 \\ & \text{s.t.} \quad \mathbf{y}^H \mathbf{y} \le 1 \\ \text{step 3:} & \mathbf{z}^{t+1} = \arg\min_{\mathbf{z}} \left\| \mathbf{s}^{t+1} - \mathbf{z} + \boldsymbol{\lambda}^t \right\|^2 \\ & \text{s.t.} \quad \|\mathbf{z} - \mathbf{s}_0\| \le \varepsilon \\ \text{step 4:} & \boldsymbol{\lambda}^{t+1} = \mathbf{s}^{t+1} - \mathbf{z}^{t+1} + \boldsymbol{\lambda}^t \\ & \boldsymbol{\gamma}^{t+1} = \mathbf{s}^{t+1} - \mathbf{y}^{t+1} + \boldsymbol{\gamma}^t \end{cases} \tag{25}$$

where t is the number of iterations. Then, solve the minimization problems (25).

For step 1, update the waveform $\mathbf{s}$. The specific algorithm is described in the next section.

$$\mathbf{s}^{t+1} = \arg\min_{\mathbf{s}} L(\mathbf{s}, \mathbf{y}^t, \mathbf{z}^t, \boldsymbol{\lambda}, \boldsymbol{\gamma}) \tag{26}$$

For step 2, the auxiliary variable $\mathbf{y}$ is updated for the fixed $\mathbf{s}$, $\mathbf{z}$, and dual variables with the most recent values. There are two conditions in this step. When a constant energy waveform design is performed, i.e., $\|\mathbf{s}\| = 1$. By using the Lagrange multiplier method, we can easily obtain the following analytical solution

$$\mathbf{y}^{t+1} = \sqrt{\frac{1}{(\mathbf{s}^{t+1} + \boldsymbol{\gamma}^t)^H (\mathbf{s}^{t+1} + \boldsymbol{\gamma}^t)}} \left(\mathbf{s}^{t+1} + \boldsymbol{\gamma}^t \right) \tag{27}$$

We consider the constraint $\|\mathbf{s}\| < 1$, the original problem transformer into a convex optimization problem, which can be solved by the CVX.

For step 3, the auxiliary variable $\mathbf{z}$ is updated for the fixed, $\mathbf{s}$, $\mathbf{y}$, and dual variables with the most recent values.

$$\begin{aligned} &\min_{\mathbf{z}} \left\| \mathbf{s}^{t+1} - \mathbf{z} + \boldsymbol{\lambda}^t \right\|^2 \\ &\text{s.t.} \|\mathbf{z} - \mathbf{s}_0\| \le \varepsilon \end{aligned} \tag{28}$$

The optimization problem of (28) is a typical convex optimization problem that can be solved by the CVX.

For step 4, the dual variables are updated utilizing fixed $\mathbf{s}$ and auxiliary variables using the most recent values.

3.2. Solution of the Waveform

DC algorithm can update the transmit waveform, which splits the non-convex objective function into the difference in two convex functions. The optimal solution to the original objective function is determined through the calculation and analysis of the two aforementioned convex functions. Moreover, the DC method provides a solution to the issue of the original non-convex objective function, which is challenging to address directly. When considering constant energy constraint, the DC algorithm can be used to directly solve for the transmit waveform with a specified energy; considering inequality energy constraint, the DC algorithm can find a lower-energy transmit waveform while ensuring smaller performance loss. The augmented Lagrangian function after simplifying (24) is

$$L(\mathbf{s}, \mathbf{y}, \mathbf{z}, \boldsymbol{\lambda}, \boldsymbol{\gamma}) = \frac{1}{2} \mathbf{s}^H \mathbf{A} \mathbf{s} + \mathrm{Re}\left\{ \mathbf{b}^H \mathbf{s} \right\} \tag{29}$$

where $\mathbf{A} = \mu \boldsymbol{\Theta}_{cn}(\mathbf{w}) - \boldsymbol{\Theta}(\mathbf{w}) - \rho \mathbf{I}$ is a non-positive definite matrix, $\mathbf{b} = \frac{\rho}{2}(\mathbf{z} - \boldsymbol{\lambda} + \mathbf{y} - \boldsymbol{\gamma})$. So, (29) is a non-convex quadratic problem, which is difficult to solve. According to the

DC decomposition, the non-convex expression can be split into the difference in two convex expressions

$$f(\mathbf{s}) = \frac{1}{2}\mathbf{s}^H\mathbf{A}\mathbf{s} + \mathbf{b}^H\mathbf{s} = g_1(\mathbf{s}) - h_1(\mathbf{s}) \tag{30}$$

where $g_1(\mathbf{s}) = \frac{1}{2}\delta\|\mathbf{s}\|^2 + \mathbf{b}^H\mathbf{s}$, $h_1(\mathbf{s}) = \frac{1}{2}\mathbf{s}^H(\delta\mathbf{I} - \mathbf{A})\mathbf{s}$, δ is a positive real number such that $\mathbf{A} + \delta\mathbf{I}$ is positive semi-definite.

Then, we can solve iteratively using the projection method. k is the number of iterations, where $\mathbf{y}^k = \delta\mathbf{s}^k$, and $\mathbf{s}^{k+1}$ is the solution of the following iterative convex quadratic programming problem

$$\min_{\mathbf{s}}\left\{\frac{1}{2}\mathbf{s}^H(\mathbf{A} + \delta\mathbf{I})\mathbf{s} + \mathbf{s}^H(\mathbf{b} - \mathbf{y}^k) : \|\mathbf{s}\| \le r\right\} \tag{31}$$

The solution of (31) is the projection of $\left(\mathbf{y}^k - \mathbf{b}\right)/\delta$ onto $E = \{\|\mathbf{s}\| \le 1\}$

$$\mathbf{s}^{k+1} = P_E\left(\mathbf{s}^k - \frac{1}{\delta}\left(\mathbf{A}\mathbf{s}^k + \mathbf{b}\right)\right) \tag{32}$$

According to the principle of the DC algorithm, we consider the quadratic normalized simplified augmented Lagrangian function

$$\begin{aligned} L(\mathbf{s}, \mathbf{y}, \mathbf{z}, \boldsymbol{\lambda}, \boldsymbol{\gamma}) &= \tfrac{1}{2}\mathbf{s}^H(\mu\boldsymbol{\Theta}_{cn}(\mathbf{w}) - \boldsymbol{\Theta}(\mathbf{w}) - \rho\mathbf{I})\mathbf{s} \\ &+ \mathrm{Re}\left\{\tfrac{\rho}{2}(\mathbf{z} - \boldsymbol{\lambda} + \mathbf{y} - \boldsymbol{\gamma})^H\mathbf{s}\right\} \end{aligned} \tag{33}$$

Let $\mathbf{A} = \mu\boldsymbol{\Theta}_{cn}(\mathbf{w}) - \boldsymbol{\Theta}(\mathbf{w}) - \rho\mathbf{I}$, $\mathbf{b} = \frac{\rho}{2}(\mathbf{z} - \boldsymbol{\lambda} + \mathbf{y} - \boldsymbol{\gamma})$, $\mathbf{s}^0 \in \mathbb{C}$ and $k = 0$.

(a) If $\| (\delta\mathbf{I} - \mathbf{A})\mathbf{s}^k - \mathbf{b} \| \le \delta$, $\mathbf{s}^{k+1} = \frac{(\delta\mathbf{I} - \mathbf{A})\mathbf{s}^k - \mathbf{b}}{\delta}$.

(b) If $\| (\delta\mathbf{I} - \mathbf{A})\mathbf{s}^k - \mathbf{b} \| > \delta$, $\mathbf{s}^{k+1} = \frac{(\delta\mathbf{I} - \mathbf{A})\mathbf{s}^k - \mathbf{b}}{\|(\delta\mathbf{I} - \mathbf{A})\mathbf{s}^k - \mathbf{b}\|}$.

If $\left\|\mathbf{s}^{k+1} - \mathbf{s}^k\right\| \le \varepsilon$, terminate. Otherwise, increase k by 1 and return to (a).

In certain scenes, the radar system may not be able to transmit waveform per unit of power. The DC algorithm is more likely than other algorithms to find an optimal solution that satisfies other constraints when considering the constraint $\|\mathbf{s}\| < 1$. Detailed procedure of ADMM for solving the waveform is summarized in Algorithm 1.

Algorithm 1: Waveform solution algorithm based on ADMM framework.

Input: α_t, α_g, $\mathbf{s}_0$, ρ, η, ζ, δ and ε;

Output: An optimized solution $\mathbf{s}^*$ to the problem (17)

1: For $t = 0$, initialize:r, $\mathbf{s}^{(t)} = \mathbf{s}_0$,$\mathbf{z}^{(t)} = \mathbf{s}^{(t)}$, $\mathbf{y}^{(t)} = \mathbf{s}^{(t)}$;

2: Compute $\mu^{(0)} = ({\mathbf{s}^{(0)}}^H\boldsymbol{\Theta}(\mathbf{w})\mathbf{s}^{(0)})/({\mathbf{s}^{(0)}}^H\boldsymbol{\Theta}_{cn}(\mathbf{w})\mathbf{s}^{(0)})$;

3: Set $t = t + 1$;

4: Update $\mathbf{s}$ by using the DC algorithm to solve the problem (26);

5: Update $\mathbf{y}$ and $\mathbf{z}$ by (27) and (28), respectively;

6: Update $\boldsymbol{\lambda}$ and $\boldsymbol{\gamma}$ by step 4 of problem (25);

7: Compute $\mu^{(t)} = ({\mathbf{s}^{(t)}}^H\boldsymbol{\Theta}(\mathbf{w})\mathbf{s}^{(t)})/({\mathbf{s}^{(t)}}^H\boldsymbol{\Theta}_{cn}(\mathbf{w})\mathbf{s}^{(t)})$;

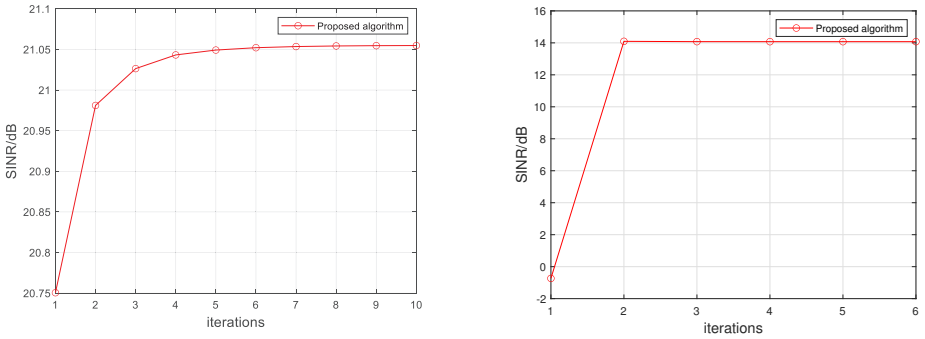
8: If $\left\|\mathbf{s}^{k+1} - \mathbf{s}^k\right\| \le \zeta$, output $\mathbf{s}^* = \mathbf{s}^{(t)}$; otherwise, repeat step 3–step 7 until convergence.

4. Numerical Examples

4.1. Evaluation of Algorithm Performance

In this section, several numerical results are provided to demonstrate the effectiveness and performance of the proposed robust joint design of transmit waveform and receive filter for MIMO radar. We consider the number of transmitting and receiving array antennas of the MIMO radar system to be $N_T = 4$, $N_R = 4$, respectively. We set the signal pulse width $T_P = 64$ μs and the bandwidth is 10 MHz. The number of pulses in a coherent processing interval is $M = 8$. The pulse repetition frequency (PRF) is $f_r = 1000$ Hz. In order to ensure the convergence of the optimized waveform, the step size is $\rho = 5000$. The error bound is $\varepsilon = 1 \times 10^{-4}$. Consider two waveform constraints; we specify the energy of the waveform in an interval, written as $\|\mathbf{s}\| \leq 1$, then, the linear frequency modulation (LFM) signal is regarded as the reference waveform of the similarity constraints. Differently, the reference waveform energy is set to 1 in the unit energy waveform design and 0.6 in the low-energy waveform design.

The effect of uncertain interference on waveform optimization in the presence of uncertain sample-length interference is considered in the first simulation experiment, where the pulse width of the sampling signal satisfies a Gaussian distribution in the range $T_L \in [3, 7]$ (μs). The sampling period is $T_S = 16$ μs. The iterative output SINR results of the uncertain interference under sample length uncertainty are shown in Figure 3.



(**a**) (**b**)

Figure 3. Iterative output SINR for ISRJ under sample-length uncertainty environment. (**a**) unit energy waveform design condition; (**b**) low-energy waveform design condition.

Figure 3a,b represents the variation curves of SINR under the unit energy waveform design condition and the low-energy waveform design condition, respectively. Simulations demonstrate that the proposed algorithm enables the cost function, which is formulated based on the probabilistic characteristics of uncertain interference, to converge to a finite value under both specified design conditions. Comparative analysis reveals that the output SINR of the low-power transmit waveform is slightly inferior to that of the full-power transmit waveform. This discrepancy is attributed to the reduction in transmit power, which results in a degradation of waveform performance and consequently leads to a decline in positioning accuracy.

In order to assess the robustness of the optimized waveform in scenarios involving uncertain interference, the optimized transmit waveforms corresponding to the sample lengths for both uncertain and deterministic interference are substituted into the random interference scenarios for Monte Carlo experiments. A total of 1000 Monte Carlo simulations are conducted, and the results are presented in Figure 4.

Figure 4a shows the input SINR-output SINR for the unit energy waveform design condition, and Figure 4b shows the input SINR-output SINR for the low-energy waveform design condition. Four different interference scenarios are considered:

1. Scenario 1 integrates the statistical properties of interference styles with different sample lengths, i.e., the uncertain interference scenario.

2. Scenario 2 considers the lowest probability of occurrence among all interference styles individually.
3. Scenario 3 considers the situation with the second highest probability of occurrence of interference.
4. Scenario 4 considers the situation with the highest probability of occurrence of interference.

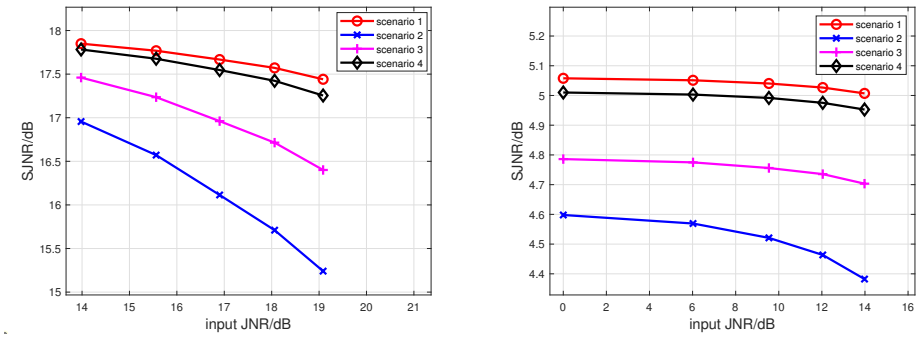


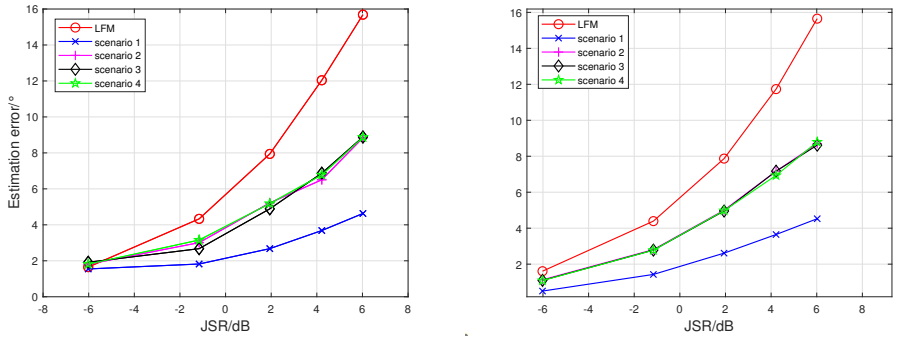
Figure 4. Comparison of the robustness of different waveforms under sample−length uncertainty environment. (**a**) unit energy waveform design condition; (**b**) low−energy waveform design condition.

A comparison of the simulation results shows that the robustness of the optimized waveform in scenario 1 is better than that of the optimized waveform in other scenarios under both unit-energy and low-energy waveform design conditions. Meanwhile, comparing the simulation results in Figure 4a,b, it is apparent that the SINR of the low-energy transmit waveform remains comparatively low.

The output waveforms under varying interference conditions are employed in the MUSIC localization algorithm to evaluate the efficacy of the proposed algorithm in localization scenarios. In a manner analogous to the robustness analysis simulation experiment previously described, the interference conditions are classified into two categories: random interference types and three deterministic interference types. Concurrently, linear frequency-modulated (LFM) signals serve as comparison waveforms to assess the performance discrepancies among the three interference conditions based on their respective localization errors concerning the target.

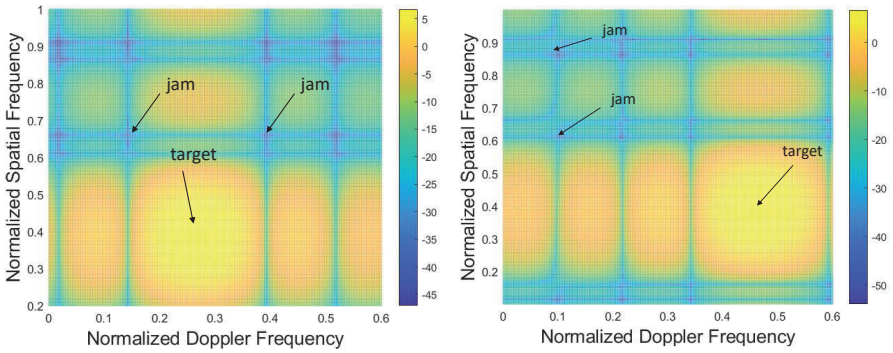
Figure 5a shows the unit energy waveform design and Figure 5b shows the low-energy waveform design. The horizontal coordinate is the interference-to-signal ratio, and the vertical coordinate is the average estimation error of target DOA calculated by the MUSIC localization algorithm for different waveforms, which are obtained by averaging 1000 Monte Carlo experiments. The simulation results show that the estimation errors of the LFM transmit waveform increase dramatically with the gradual increase in the interference energy, which is due to the fact that they are not processed with anti-jamming, resulting in the degradation of the localization performance. Comparatively speaking, the optimized waveforms are affected by the interference with less variation, in which the optimized waveform considering random interference performs better than the transmit waveform designed under deterministic interference conditions.

Figure 6 illustrates the temporal cross-ambiguity of the two waveforms under conditions of sample-length uncertainty. Specifically, Figure 6a presents the design of a unit energy waveform, while Figure 6b depicts the low-energy waveform design. The simulation results indicate that both the unit energy and low-energy waveform designs exhibit a prominent main lobe near the target, which effectively creates a noticeable depression in close proximity to the interference, thereby suppressing it. Consequently, the integrated design of the waveform and filter can mitigate the interference power to an acceptable level, while simultaneously ensuring that adequate transmission power is maintained in the direction of the target. This approach serves to enhance the radar's suppression of interference.



(**a**) (**b**)

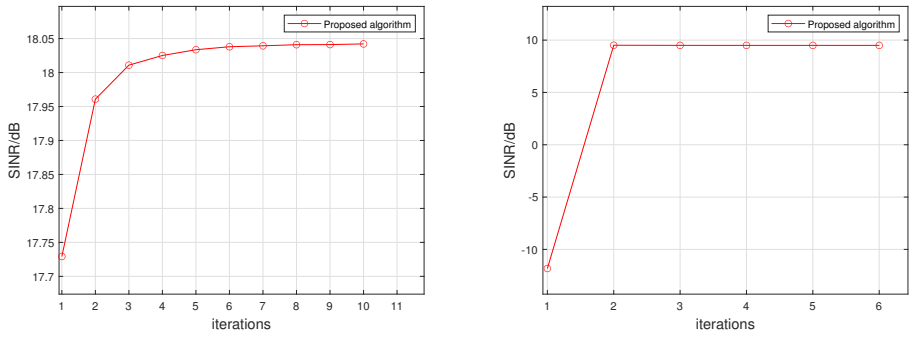
Figure 5. Estimation error of different waveforms regarding DOA localization. (**a**) unit energy waveform design condition; (**b**) low-energy waveform design condition.



(**a**) (**b**)

Figure 6. Interference spectra under uncertain sample-length environment. (**a**) unit energy waveform design condition; (**b**) low-energy waveform design condition.

In the second simulation experiment, the effect of uncertain interference on waveform optimization in the presence of uncertainty in sample time is considered, where the pulse width of the sampling signal is $T_L = 7$ μs. The sampling period satisfies a Gaussian distribution in the range $T_S \in [17, 21]$ (μs). The iterative output SINR results of uncertain interference under sample-time uncertainty are shown in Figure 7.



(**a**) (**b**)

Figure 7. Iterative output SINR for ISRJ under sample-time uncertainty environment. (**a**) unit energy waveform design condition; (**b**) low-energy waveform design condition.

Figure 7a,b illustrates the variations in SINR corresponding to the unit-energy waveform design condition and the low-energy waveform design condition, respectively. Analogous to the scenario involving uncertain interference sample length, the proposed algorithm facilitates the convergence of the cost function—constructed using the probabilistic characteristics of random interference—to a finite value, even under conditions of uncertain

sample time for both design scenarios. Comparative analysis indicates that the output SINR of the low-power transmit waveform remains marginally inferior to that of the full-power transmit waveform. To evaluate the robustness of the optimized waveform under scenarios of random interference, the optimized transmit waveforms designed for both uncertain and deterministic interference sampling time will be tested within random interference environments. This will be conducted through Monte Carlo experiments, with a total of 1000 iterations set for the simulations. The results are shown in Figure 8.

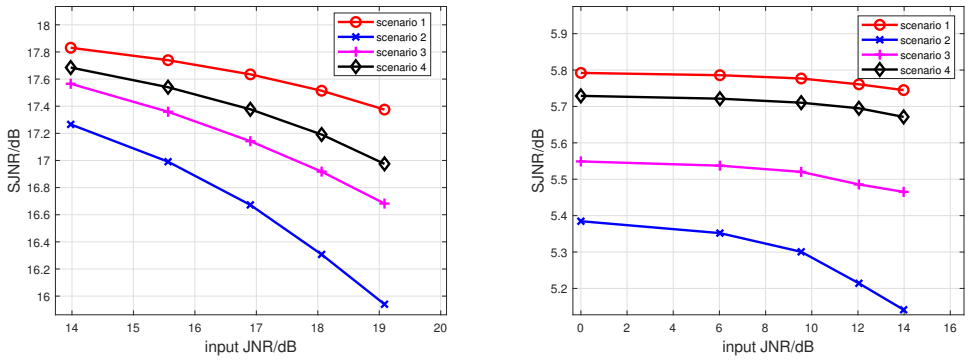


Figure 8. Comparison of the robustness of different waveform under sampling time uncertainties. (**a**) unit energy waveform design condition; (**b**) low-energy waveform design condition.

Figure 8a illustrates the relationship between input SINR and output SINR under conditions of unit energy waveform design, while Figure 8b depicts this relationship for low-energy waveform design. The specific simulation scenarios are similar to those with uncertainty in sample length. Comparison of the simulation results indicates that the robustness of the optimized waveform outperforms that of the waveform optimized under definitive interference conditions for both unit-energy and low-energy waveform design scenarios. Furthermore, an analysis of the simulation results presented in Figure 8a,b reveals that the SINR of the low-energy transmit waveform remains comparatively low.

Similarly, the output waveforms corresponding to various interference conditions are employed in the MUSIC localization algorithm to assess the efficacy of the proposed method within the localization framework. Consistent with the robustness analysis simulation experiment previously described, the interference conditions are classified into random interference and three types of deterministic interference. Additionally, LFM signals serve as reference waveforms to evaluate the performance differences among the three interference conditions based on their localization errors concerning the target.

Figure 9a illustrates the design of the unit-energy waveform, while Figure 9b depicts the design of the low-energy waveform. The horizontal axis represents the jamming-to-signal ratio (JSR), and the vertical axis denotes the average estimation error of the target Direction of Arrival (DOA), as calculated by the MUSIC localization algorithm for various waveforms. These results are derived from the averaging of 1000 Monte Carlo simulations. The simulation findings indicate that the estimation errors associated with the LFM transmit waveform increase significantly as the interference energy rises. This deterioration in localization performance is attributed to the absence of anti-jamming processing. In contrast, the optimized waveform exhibits less variation under interference conditions, with those designed to account for uncertain interference outperforming those developed under deterministic interference scenarios.

Figure 10 illustrates the temporal cross-ambiguity of two waveforms under conditions of sample-time uncertainty. Specifically, Figure 10a presents the unit energy waveform design, whereas Figure 10b showcases the low-energy waveform design. The simulation results indicate that both the unit-energy and low-energy waveform designs exhibit a main lobe near the target, accompanied by a distinct depression in the vicinity of the interference,

effectively suppressing it. Consequently, the integrated approach of waveform and filter design enables a reduction in interference power to an acceptable level while maintaining adequate transmission power directed toward the target. This strategy enhances the receiver's resilience against interference, thereby improving overall performance.

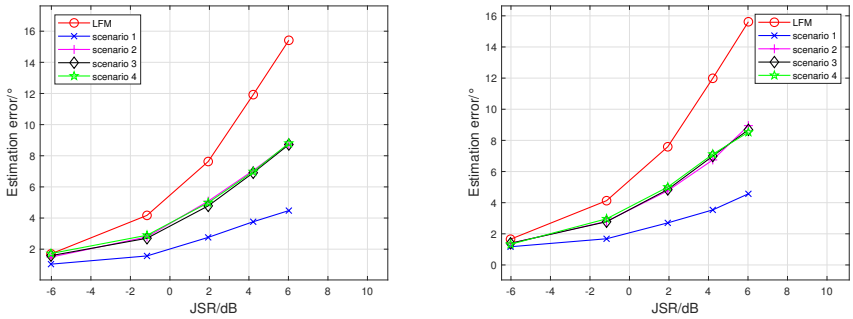


Figure 9. Estimation error of different waveform regarding DOA localization. (**a**) unit energy waveform design condition; (**b**) low-energy waveform design condition.

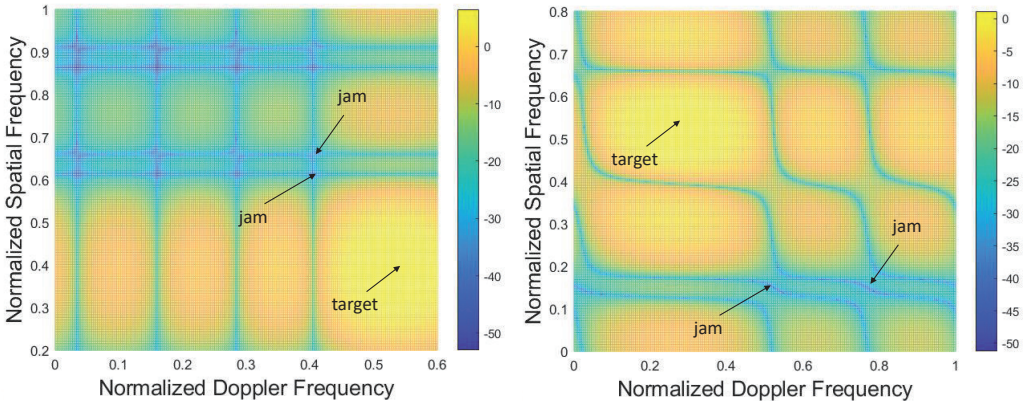


Figure 10. Interference spectra under uncertainty of sample time. (**a**) unit energy waveform design condition; (**b**) low-energy waveform design condition.

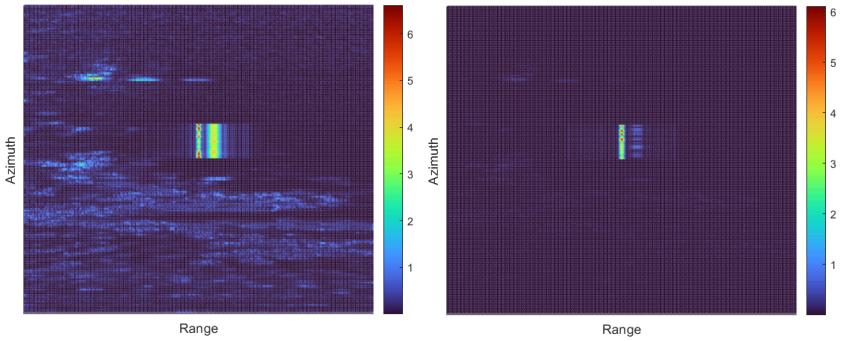
In summary, whether the sample length is uncertain or the sample time is uncertain, the robustness of the optimized waveform consistently surpasses that of the optimized waveform under deterministic interference conditions when accounting for the random distribution characteristics of the interference. Furthermore, it is demonstrated that the robust waveform design algorithm proposed in this article is capable of effectively addressing the complexities and parameter variability associated with future radar electronic warfare environments.

4.2. SAR Anti-Interference Real Scene Imaging Simulation

In this section, the real scene imaging simulations are conducted to evaluate the performance of the uncertain ISRJ suppression. To adequately show the echoes of heterogeneous ground clutter, we adopt real data of clutter amplitudes of an X-band radar McMaster IPIX Radar. The complex image with a single view is utilized to model the backscattering coefficient, and the echo is generated point by point. SAR simulation parameters are as follows. The carrier frequency and the bandwidth are 5.4 GHz and 10 MHz, respectively. The sampling period of uncertain sample length ISRJ is $T_S = 32$ us, and the pulse width of the sampling signal satisfies a Gaussian distribution in the range $T_L \in [6, 14]$ (us). Considering the sample-time uncertainty, the pulse width of the sampling signal is $T_L = 10$ us, and the sampling period satisfies a Gaussian distribution in the range $T_S \in [15, 20]$ (us).

In the real scene imaging simulation, the velocity in the azimuth direction is 80 m/s. The JSR is set as 30 dB.

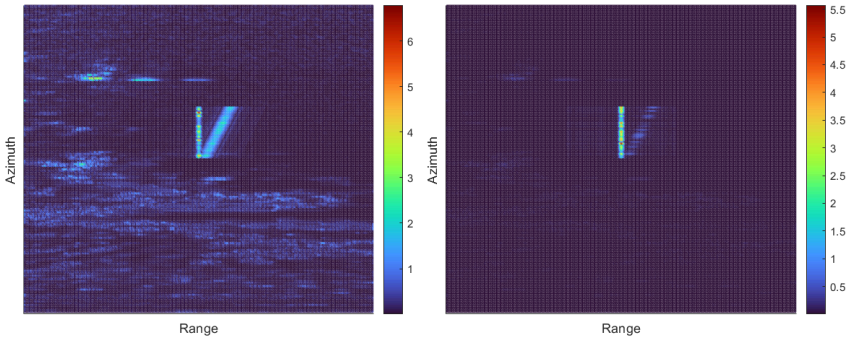
Figure 11a shows the imaging results when the MIMO-SAR is jammed by the uncertain ISRJ. And the velocity of the false targets is the same as the true target. The deception targets are clearly visible on the image by applying the time-frequency filtering method. We can observe that the false targets have a serious impact on MIMO-SAR imaging. The effective uncertain ISRJ suppression and MIMO-SAR imaging performance are shown in Figure 11b. The deception false targets are effectively filtered out, which demonstrates that the proposed method can suppress the processing gain of the jamming peak.



(**a**) (**b**)

Figure 11. Imaging results in the presence of uncertain ISRJ. (**a**) image without uncertain ISRJ suppression; (**b**) image obtained using waveform of the proposed method.

The second scene imaging simulation is shown in Figure 12a.We impose dragging jamming to MIMO-SAR images, which creates different interference effects in MIMO-SAR imaging. The JSR is set as 30 dB and the rest of the parameters are the same as those in the first simulation. As shown in Figure 12a, all true targets are obtained in the imaging results. However, the false targets are generated and the interference amplitude is larger than the true targets. This can be explained by the fact that the interference peak level is coherent without anti-interference processing. It can achieve the azimuth processing gain after range bin migration. As is shown in Figure 12b, by utilizing the designed waveform of the proposed method, the amplitude of uncertain ISRJ peak is obviously reduced. In other words, the jamming peak level can only obtain partial azimuth processing gain by using the designed waveform.



(**a**) (**b**)

Figure 12. Imaging results in the presence of uncertain ISRJ. (**a**) image without uncertain ISRJ suppression; (**b**) image obtained using waveform of the proposed method.

5. Conclusions

In order to enhance the output SINR performance of the MIMO-SAR system, this article addresses the issue of robust joint design for both the MIMO-SAR waveform and filter under an uncertain interference environment. Specifically, we formulate a statistical

matrix that characterizes the random distribution of the interference signals. Subsequently, we develop a non-convex optimization problem aimed at designing an anti-interference transmit waveform, incorporating energy and similarity constraints, with the output SINR serving as the optimization criterion. To address the non-convex constraints within the ADMM algorithm, we introduce the DC-programming as an alternative solution, ensuring the convergence of the ADMM approach. Numerical examples are provided to demonstrate the effectiveness of the proposed algorithm. The results indicate that the performance of the designed waveform consistently exceeds that of scenarios that do not account for the random distribution characteristics of the interference. Furthermore, when performing DOA estimation using the MUSIC algorithm, the waveforms designed under the consideration of interference characteristics exhibit lower estimation errors compared to those designed without such considerations.

Author Contributions: Conceptualization, K.X. and Z.D.; Methodology, K.X. and G.S.; Software, W.C.; Data curation, Y.J.; Writing—original draft, K.X.; Writing—review & editing, K.X. All authors have read and agreed to the published version of the manuscript.

Funding: This work was supported in part by the National Natural Science Foundation of China under Grant No. 62201371, the Sichuan Science and Technology Program No. 2023NSFSC1382, and the Opening Project of Robotic Satellite Laboratory.

Data Availability Statement: The raw data supporting the conclusions of this article will be made available by the authors on request.

Conflicts of Interest: The authors declare no conflicts of interest.

References

1. Li, G.; Lu, Q.; Ye, W. Research on Anti-interference Performance of Sparsity-based SAR Imaging. In Proceedings of the 2019 IEEE 4th International Conference on Signal and Image Processing (ICSIP), Wuxi, China, 19–21 July 2019 ; IEEE: Piscataway, NJ, USA, 2019; pp. 592–596.
2. Çetin, M.; Stojanović, I.; Önhon, N.Ö.; Varshney, K.; Samadi, S.; Karl, W.C.; Willsky, A.S. Sparsity-driven synthetic aperture radar imaging: Reconstruction, autofocusing, moving targets, and compressed sensing. *IEEE Signal Process. Mag.* **2014**, *31*, 27–40. [CrossRef]
3. Pu, W. Deep SAR imaging and motion compensation. *IEEE Trans. Image Process.* **2021**, *30*, 2232–2247. [CrossRef] [PubMed]
4. Lin, B.; Li, C.; Ji, Y.; Zhang, W.; Yuan, Y.; Liu, X.; Fang, G. An Efficient Range Scaling Algorithm for MIMO-SAR 3-D Imaging. *IEEE Trans. Microw. Theory Tech.* **2024**, *72*, 4945–4959. [CrossRef]
5. Tan, Y.; Li, Z.; Yang, J.; Yu, X.; An, H.; Wu, J.; Yang, J. Joint communication and sar waveform design method via time-frequency spectrum shaping. *IEEE Trans. Geosci. Remote Sens.* **2022**, *60*, 1–13. [CrossRef]
6. Zhou, K.; Li, D.; Quan, S.; Liu, T.; Su, Y.; He, F. SAR waveform and mismatched filter design for countering interrupted-sampling repeater jamming. *IEEE Trans. Geosci. Remote Sens.* **2021**, *60*, 1–14. [CrossRef]
7. Wang, Y.; Zhan, X.; Gao, J.; Yao, J.; Wei, S.; Bai, J. Array SAR 3D Sparse Imaging Based on Regularization by Denoising Under Few Observed Data. *IEEE Trans. Geosci. Remote Sens.* **2024**, *62*, 5213114.
8. Wang, Y.; He, Z.; Zhan, X.; Zeng, Q.; Hu, Y. A 3-D sparse SAR imaging method based on plug-and-play. *IEEE Trans. Geosci. Remote. Sens.* **2022**, *60*, 1–14. [CrossRef]
9. Wang, Y.; He, Z.; Zhan, X.; Fu, Y.; Zhou, L. Three-dimensional sparse SAR imaging with generalized L q regularization. *Remote Sens.* **2022**, *14*, 288. [CrossRef]
10. Yang, K.; Ye, W.; Wu, X.; Ma, F.; Li, G. Fast generation of deceptive jamming signal against space-borne SAR. *IEEE J. Sel. Top. Appl. Earth Obs. Remote Sens.* **2020**, *13*, 5580–5596. [CrossRef]
11. Wang, X.; Liu, J.; Zhang, W.; Fu, Q.; Liu, Z.; Xie, X. Mathematic principles of interrupted-sampling repeater jamming (ISRJ). *Sci. China Ser. F Inf. Sci.* **2007**, *50*, 113–123. [CrossRef]
12. Lin, H.; Xing, M.; Lou, Y.; Wang, Z.; Zhang, T.; Sun, G. Research on Anti-Deception Forwarding Interference of Squint Azimuth Multi-channel SAR. *IEEE Trans. Geosci. Remote Sens.* **2023**, *62*, 5203912.
13. Zhou, K.; Su, Y.; Wang, D.; Ma, H.; Liu, L.; Li, C. Improved SAR interrupted-sampling repeater jamming countermeasure based on waveform agility and mismatched filter design. *IEEE Trans. Geosci. Remote Sens.* **2023**, *61*, 1–16. [CrossRef]
14. Kong, Y.; Xia, S.; Dong, L.; Yu, X.; Cui, G. Compound Jamming Recognition via Contrastive Learning for Distributed MIMO Radars. *IEEE Trans. Veh. Technol.* **2024**, *73*, 7892–7907. [CrossRef]
15. Bang, H.; Wang, W.Q.; Zhang, S.; Liao, Y. FDA-based space–time–frequency deceptive jamming against SAR imaging. *IEEE Trans. Aerosp. Electron. Syst.* **2021**, *58*, 2127–2140. [CrossRef]

16. Wei, J.; Li, Y.; Yang, R.; Zhu, E.; Ding, J.; Ding, M.; Zhang, P. A Time Domain Filtering Method Based on Intra-pulse Joint Inter-pulse Coding to Counter Interrupted Sampling Repeater Jamming in SAR. *IEEE Trans. Geosci. Remote Sens.* **2023**, *61*, 5215912. [CrossRef]
17. Lee, H.; Kim, K.W. Effective Barrage Noise Jamming for Spotlight SAR Using Extended Kalman Filter-Based Kinematic Parameter Estimation. *IEEE J. Sel. Top. Appl. Earth Obs. Remote Sens.* **2023**, *16*, 6579–6600. [CrossRef]
18. Wang, Y.; Jin, G.; Song, C.; Lu, P.; Han, S.; Lv, J.; Zhang, Y.; Wu, D.; Zhu, D. Parameterized and large-dynamic-range 2-D precise controllable SAR jamming: Characterization, modeling, and analysis. *IEEE Trans. Geosci. Remote Sens.* **2023**, *61*, 1–16. [CrossRef]
19. Tang, B.; Tang, J. Joint design of transmit waveforms and receive filters for MIMO radar space-time adaptive processing. *IEEE Trans. Signal Process.* **2016**, *64*, 4707–4722. [CrossRef]
20. Zhou, J.; Li, H.; Cui, W. Biquadratic optimization based joint transmit and receive beamforming with sequential rank relaxation. *Signal Process.* **2021**, *179*, 107819. [CrossRef]
21. Wang, L.; Zhu, W.; Zhang, Y.; Liao, Q.; Tang, J. Multi-target detection and adaptive waveform design for cognitive MIMO radar. *IEEE Sensors J.* **2018**, *18*, 9962–9970. [CrossRef]
22. De Maio, A.; De Nicola, S.; Huang, Y.; Zhang, S.; Farina, A. Code design to optimize radar detection performance under accuracy and similarity constraints. *IEEE Trans. Signal Process.* **2008**, *56*, 5618–5629. [CrossRef]
23. Ge, M.; Yu, X.; Yan, Z.; Cui, G.; Kong, L. Joint cognitive optimization of transmit waveform and receive filter against deceptive interference. *Signal Process.* **2021**, *185*, 108084. [CrossRef]
24. Zhou, K.; Li, D.; Su, Y.; Liu, T. Joint design of transmit waveform and mismatch filter in the presence of interrupted sampling repeater jamming. *IEEE Signal Process. Lett.* **2020**, *27*, 1610–1614. [CrossRef]
25. Zhang, J.; Zhu, D.; Zhang, G. New antivelocity deception jamming technique using pulses with adaptive initial phases. *IEEE Trans. Aerosp. Electron. Syst.* **2013**, *49*, 1290–1300. [CrossRef]
26. Akhtar, J. Orthogonal block coded ECCM schemes against repeat radar jammers. *IEEE Trans. Aerosp. Electron. Syst.* **2009**, *45*, 1218–1226. [CrossRef]
27. Guerci, J.R. Cognitive radar: A knowledge-aided fully adaptive approach. In Proceedings of the 2010 IEEE Radar Conference, Arlington, VA, USA, 10–14 May 2010; IEEE: Piscataway, NJ, USA, 2010; pp. 1365–1370.
28. Xiong, W.; Wang, X.; Zhang, G. Cognitive waveform design for anti-velocity deception jamming with adaptive initial phases. In Proceedings of the 2016 IEEE Radar Conference (RadarConf), Philadelphia, PA, USA, 2–6 May 2016; IEEE: Piscataway, NJ, USA, 2016; pp. 1–5.
29. Zhang, H.; Zhu, Y.; Feng, J.; Fu, Q. Nonuniform ISRJ suppression based on time shift alignment and morphological processing. In Proceedings of the 2022 3rd International Conference on Signal Processing and Computer Science (SPCS 2022), Qingdao, China, 19–22 August 2022, Journal of Physics: Conference Series; IOP Publishing: Bristol, UK, 2022; Volume 2414, p. 012010.
30. Sun, Z.; Quan, Y.; Liu, Z. A non-uniform interrupted-sampling repeater jamming method for intra-pulse frequency agile radar. *Remote Sens.* **2023**, *15*, 1851. [CrossRef]
31. Zhu, J.; Xie, Z.; Jiang, N.; Song, Y.; Han, S.; Liu, W.; Huang, X. Delay-Doppler map shaping through oversampled complementary sets for high-speed target detection. *Remote Sens.* **2024**, *16*, 2898. [CrossRef]
32. Wu, Q.; Zhao, F.; Wang, J.; Liu, X.; Xiao, S. Improved ISRJ-based radar target echo cancellation using frequency shifting modulation. *Electronics* **2019**, *8*, 46. [CrossRef]
33. Chuanzhang, W.; Baixiao, C. Study on generating method of interrupted non-uniform sampling repeater jamming. *Syst. Eng. Electron.* **2021**, *43*, 7–16.
34. Tang, Q.; Rong, J. Research on the Random Interrupted Sampling Loop Repeater Jamming method of LFM. In Proceedings of the 2023 6th International Conference on Artificial Intelligence and Pattern Recognition, Xiamen, China, 22–24 September 2023; pp. 1110–1115.
35. Li, Z.; Shi, J.; Liu, W.; Pan, J.; Li, B. Robust joint design of transmit waveform and receive filter for MIMO-STAP radar under target and clutter uncertainties. *IEEE Trans. Veh. Technol.* **2021**, *71*, 1156–1171. [CrossRef]
36. Xu, C.; Yu, L.; Wei, Y.; Tong, P. Research on active jamming recognition in complex electromagnetic environment. In Proceedings of the 2019 IEEE International Conference on Signal, Information and Data Processing (ICSIDP), Chongqing, China, 11–13 December 2019; IEEE: Piscataway, NJ, USA, 2019; pp. 1–5.
37. Zhu, J.; Song, Y.; Jiang, N.; Xie, Z.; Fan, C.; Huang, X. Enhanced Doppler resolution and sidelobe suppression performance for Golay complementary waveforms. *Remote Sens.* **2023**, *15*, 2452. [CrossRef]
38. Tang, B.; Li, J.; Zhang, Y.; Tang, J. Design of MIMO radar waveform covariance matrix for clutter and jamming suppression based on space time adaptive processing. *Signal Process.* **2016**, *121*, 60–69. [CrossRef]
39. Pavez, E.; Ortega, A. Covariance matrix estimation with non uniform and data dependent missing observations. *IEEE Trans. Inf. Theory* **2020**, *67*, 1201–1215. [CrossRef]

Disclaimer/Publisher's Note: The statements, opinions and data contained in all publications are solely those of the individual author(s) and contributor(s) and not of MDPI and/or the editor(s). MDPI and/or the editor(s) disclaim responsibility for any injury to people or property resulting from any ideas, methods, instructions or products referred to in the content.